Stability field and thermal equation of state of ε-iron determined by synchrotron X-ray diffraction in a multianvil apparatus

Takeyuki Uchida, Yanbin Wang, Mark L. Rivers, and Stephen R. Sutton

Consortium for Advanced Radiation Sources, University of Chicago, Chicago, Illinois, USA

Abstract. In situ synchrotron X-ray diffraction measurements have been carried out on Fe using a "T cup" multianvil high-pressure apparatus up to 20 GPa and 1500 K. The stability field of the hexagonal phase (ε-Fe) is characterized by the triple point of the body-centered cubic (bcc) (α), ε, and face-centered cubic (fcc) (γ) phases, located at 8.0($\pm$0.3) GPa and 680($\pm$50) K with the slope of the phase boundary between the ε and γ phases being 36 ± 3 K GPa^{-1}. Pressure-volume-temperature (P-V-T) data for the ε-Fe enable us to extract thermal equation of state (EOS) parameters accurately. Least squares fit of a combination of our room temperature data with previous results using the diamond anvil cell (DAC) to the third-order Birch-Murnaghan EOS yields $K_{T,0} = 135 \pm 19$ GPa, $K'_{T,0} = 6.0 \pm 0.4$, and $V_0 = 22.7 \pm 0.3$ Å^3, where $K_{T,0}$, $K'_{T,0}$, and V_0 are zero-pressure isothermal bulk modulus, its pressure derivative, and zero-pressure volume, respectively. Volume data at high temperatures are fit with various high-temperature EOSs. A fit using the high-temperature Birch-Murnaghan EOS yields the temperature derivative of the bulk modulus $(\partial K_{T,0}/\partial T)_P = -4.48 \pm 0.56 \times 10^{-2}$ GPa K^{-1}, with the zero-pressure thermal expansivity in the form $\alpha_{T,0} = a + bT - cT^{-2}$, where $a = 3.98 \pm 0.24 \times 10^{-5}$ K^{-1}, $b = 5.07 \pm 0.88 \times 10^{-8}$ K^{-2}, and c is nonresolvable from 0. The thermal pressure approach based on the Mie-Grüneisen-Debye theory gives $(\alpha_{T,0}K_{T,0})$ and $(\partial^2 P/\partial T^2)_V$ to be $6.88 \pm 0.30 \times 10^{-3}$ GPa K^{-1} and $4.63 \pm 0.53 \times 10^{-6}$ GPa K^{-2}, respectively. The thermoelastic parameters obtained from various EOSs are mutually consistent. The edge lengths (a and c) for the ε-Fe are also fit with the Mie-Grüneisen-Debye EOS based on fictitious volumes (a^3 and c^3, respectively) to obtain pressure and temperature dependence of c/a. Linear thermal expansivity for the c axis is slightly larger than that of the a axis while incompressibilities are similar. Thus pressure dependence of c/a at each temperature is quite similar, although absolute values of c/a become higher with increasing temperature. Below 20 GPa, no new phase between the ε- and γ-Fe stability fields was observed, and no anomaly in the c/a ratio was detected. Under the assumption that ε-Fe is stable at the corresponding P and T conditions of the Earth's inner core, the density of ε-Fe is significantly higher than that of the Preliminary Reference Earth Model, indicating light element(s) must be present not only in the outer core but also in the inner core.

1. Introduction

The Earth's core consists of a liquid outer core and a solid inner core [e.g., *Dziewonski and Anderson*, 1981], which are believed to be made predominantly of iron (Fe) [e.g., *Birch*, 1952, 1964]. Crystal structure, melting temperature, and equation of state (EOS) of Fe therefore provide important clues to infer the composition and the thermodynamic state of the core. Heating at room pressure changes the structure of Fe sequentially from body-centered cubic (bcc) (α phase) to bcc (β phase) [*Mirwald and Kennedy*, 1979; *Besson and Nicol*, 1990], face-centered cubic (fcc) (γ phase), bcc (δ phase), and liquid. The transition from α to β is associated only with a magnetism change from ferromagnetic to paramagnetic without structural and volume change [*Basinski et al.*, 1955]. Compression of the α phase at room temperature causes the transformation to hexagonal close packed (hcp) (ε phase) at ~11 GPa [*Mangh-

nani et al.*, 1987; *Huang et al.*, 1987], and heating the ε phase at high pressure results in a transition to the γ phase [e.g., *Akimoto et al.*, 1987; *Mao et al.*, 1987; *Boehler et al.*, 1987]. The triple point of α, ε, and γ phases is reported to be at 8.3 GPa and 713 K on the basis of phase equilibrium study using a cubic-type multianvil apparatus [*Akimoto et al.*, 1987]. On the basis of in situ synchrotron diffraction in the diamond anvil cell (DAC), *Manghnani et al.* [1987] and *Huang et al.* [1987] reported negative slopes for the α-ε boundary, while *Akimoto et al.* [1987] gave a positive slope in their experiments using a cubic anvil press. *Shen et al.* [1998] reported a ε-γ-liquid triple point at 60($\pm$5) GPa and 2800($\pm$200) K in DAC experiments. Recently, the existence of a new high P and T phase (so-called β phase) has been suggested [*Saxena and Dubrovinsky*, 2000, and references therein; *Andrault et al.*, 1997, 2000].

The melting temperature of Fe provides important constraints on the temperature at the inner core and outer core boundary (IOB) [e.g., *Stevenson*, 1981; *Poirier*, 1994] and has been examined by several researchers using both shock wave [*Brown and McQueen*, 1986; *Williams et al.*, 1987; *Yoo et al.*, 1993] and static compression [*Boehler*, 1993; *Shen et al.*, 1998].
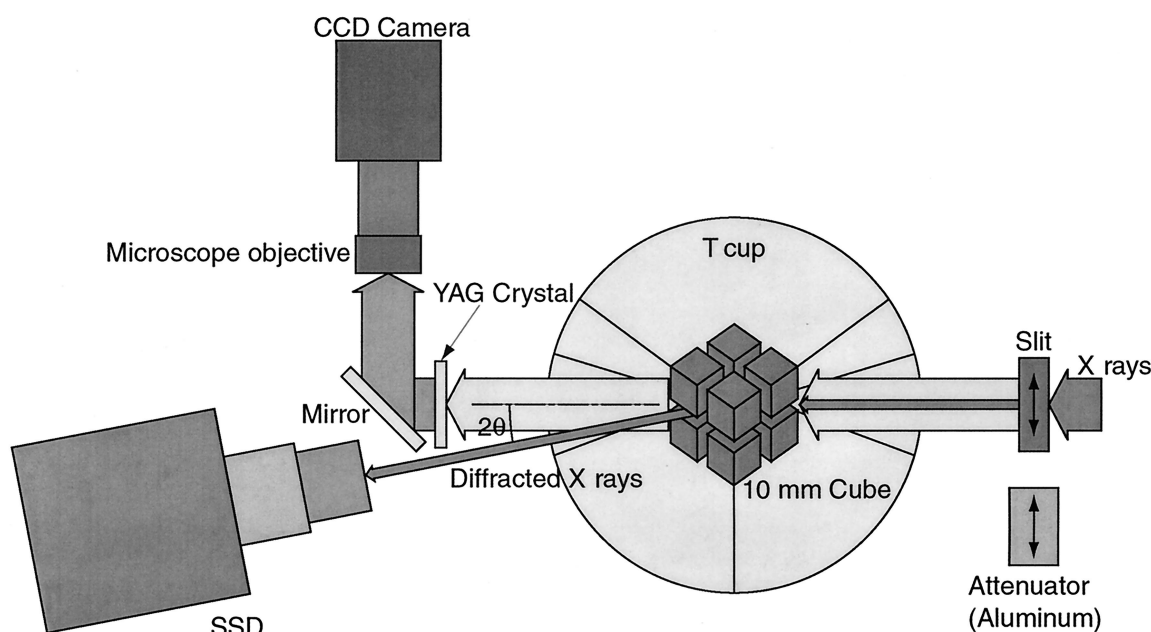
Figure 1. Schematic illustration of X-ray diffraction and imaging setup (top view). Diffracted X rays travel above the YAG and mirror assembly and are detected by the pure Ge solid-state detector (SSD) with a fixed diffraction angle 2θ of 6.0°. Transmitted X rays are converted by the YAG single-crystal phosphor to visible light, which is then reflected by the mirror through the microscope objective into the CCD camera. Diffraction and imaging modes are interchanged by driving the incident slits in (diffraction) and out (imaging) of the incident beam path. Using this imaging setup, we can identify the optimum sample position in the vertical plane, which is perpendicular to the plane of this picture. The sample position is centered by scanning the sample in the axis (along this paper) parallel to X-ray direction.

Williams et al. [1987] reported a melting curve and estimated the IOB temperature to be 7600 ± 500 K by extrapolation. *Yoo et al.* [1993] reported a lower melting curve and estimated the temperature to be 6830 K, which is still higher than that reported by *Brown and McQueen* [1986] (5800 K). Melting curves proposed by *Williams et al.* [1987] and *Yoo et al.* [1993] are also significantly higher than that obtained by static compression in the DAC [*Boehler*, 1993]. The melting temperature reported by *Shen et al.* [1998] is in good agreement with that reported by *Boehler* [1993] below 60 GPa, but the temperature at IOB was not estimated. First principles and molecular dynamic simulations of ε-Fe estimate that the temperature at IOB pressure (330 GPa) is 5400 ± 400 K [*Laio et al.*, 2000].

Several EOS data sets exist from previous DAC studies. Room temperature EOS of ε phase has been studied in the DAC by *Mao and Bell* [1979], *Mao et al.* [1990], and *Jephcoat et al.* [1986] up to 94, 300, and 78 GPa, respectively. The high-temperature EOS was studied by *Dubrovinsky et al.* [1998a, 2000] up to 68 GPa with a wire-heating technique in the DAC [*Dubrovinsky et al.*, 1998a] and to 300 GPa with externally heated DAC [*Dubrovinsky et al.*, 2000]. The laser-heated diamond anvil cell (LHDAC) covers a wide pressure and temperature range and can produce *P-T* conditions corresponding to the center of the Earth. Despite its suitability for generating high *P* and *T* conditions, Fe phase diagrams reported using the LHDAC show large variations (see reviews by *Shen et al.* [1998] and *Anderson and Isaak* [2000]).

Compared to the DAC, the pressure and temperature range is more restricted in the large volume press (LVP); however, there are several advantages. The large sample volume yields better counting statistics and consistent signal quality; the internal resistance heater generates a uniform temperature environment for both the sample and the pressure standard; and heating characteristics are independent of sample or heater materials. Thus more reliable *P-V-T* data for EOS can be collected in the LVP. Using a MA8-type high-pressure apparatus, *Funamori et al.* [1996] reported thermal expansivities for the ε- and γ-Fe at high *P*, but the number of data points is insufficient to extract the complete thermoelastic EOS.

In the present study, we use a "T cup" multianvil apparatus to establish the stability field and EOS of ε-Fe up to 20 GPa and 1500 K, combined with the synchrotron X radiation at the Advanced Photon Source (APS). The stability field of Fe is characterized by the location of the α-ε-γ triple point and the ε-γ boundary. Room temperature data for ε-Fe are compared to previous DAC data and combined together to obtain the most suitable room temperature compression curve, which is used as a reference baseline in the high-temperature data fit. The high-temperature data are fitted to several high-temperature EOSs to extract a thermal expansivity of ε-Fe. The resultant EOS parameters are compared to those obtained by *Funamori et al.* [1996] and *Dubrovinsky et al.* [1998a, 2000]. The accuracy of our new data allows us to examine structural distortion (represented by the *c/a* ratio), as a function of *P* and *T*. The density of ε-Fe is then calculated from the EOS of pure ε-Fe at the Earth's core conditions. Comparison to the density of Preliminary Reference Earth Model (PREM) [*Dziewonski and Anderson*, 1981] provides constraints on the possible presence of light element(s) in the Earth's core.

(a)   (b)
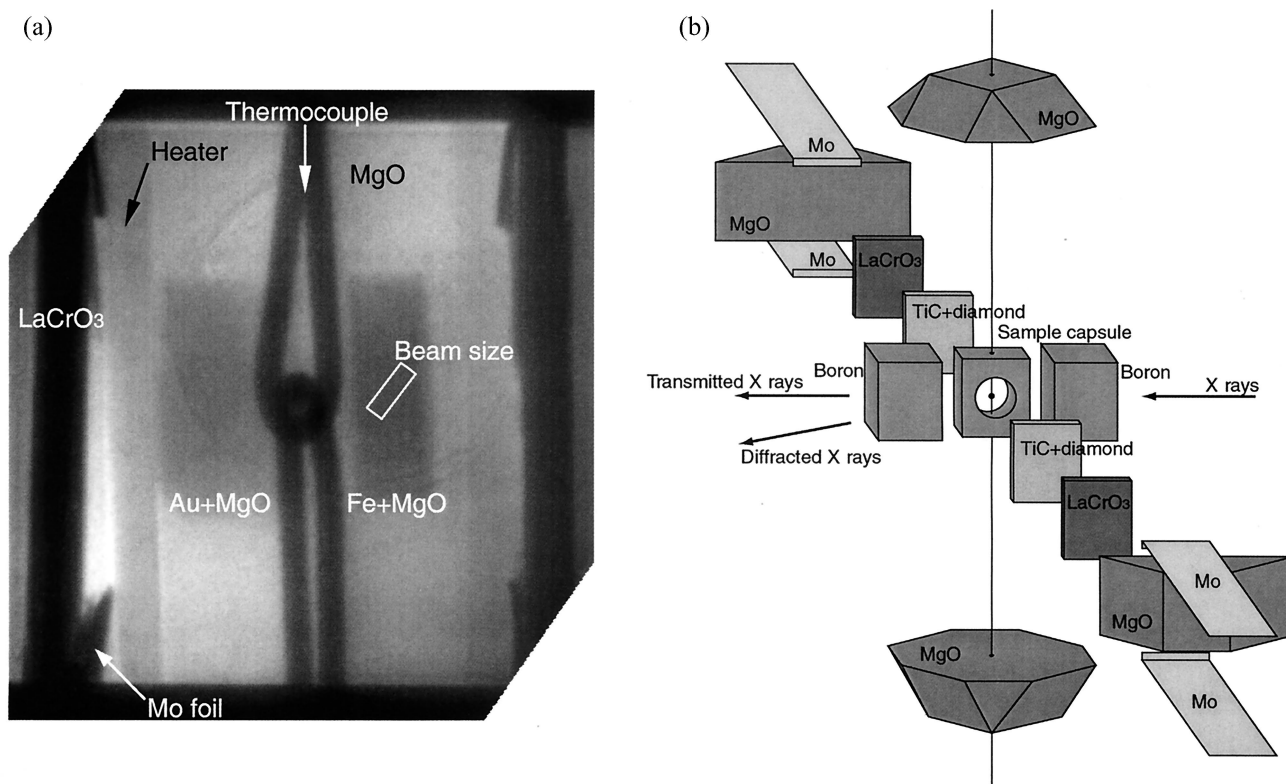

Figure 2. Cell assembly for (a) X-ray image at ambient condition and (b) schematic configuration of cell parts. In the X-ray path a mixture of boron and epoxy resin (4:1 in weight) is employed to minimize X-ray absorption and to avoid contamination by other X-ray diffraction lines. Mixtures of Au and MgO and Fe and MgO, with higher X-ray absorption coefficients than the surrounding MgO sample container, were packed in the hole and embedded the thermocouple. To avoid contact between Fe and thermocouple or heater, a thin layer of MgO is also inserted into the chamber, as can be seen as small contrast difference. The sample and pressure standard are heated with an internal resistance heater made of a mixture of TiC and diamond powders. To improve heating efficiency, LaCrO$_3$ plates are put between heater and pressure medium MgO.

2. Experimental Technique

High P and T in situ X-ray diffraction was performed using the 250-t press [*Wang et al.*, 1998] installed at the GSECARS 13-BM-D beam line [*Rivers et al.*, 1998] at the APS, with the T cup multianvil apparatus [*Vaughan et al.*, 1998]. The apparatus consists of eight cube-shaped inner anvils (10 mm edge length), made of cemented tungsten carbide with a truncated edge length of 2.0 mm, and of six outer split-cylinder-type anvils that form a cubic cavity with an edge length of 18 mm. The compression axis of the 250-t press is along the [111] direction of the cubic cavity that is filled with the inner anvils. The diffraction vector is inclined by 35.26° from the vertical loading axis, and X-ray access is through gaps between the inner anvils. In situ X-ray diffraction measurements were carried out using the energy dispersive method with an energy range of 20–100 keV. Incident X rays were collimated to 100×300 μm by two pairs of tungsten carbide slits (entrance slits), and diffracted X rays were detected by a Ge solid-state detector at a fixed diffraction angle of 6°. Transmitted X rays were converted to visible light by a yttrium/aluminum/garnet (YAG) crystal and the light was reflected by a mirror at a 90° angle. The reflected visible light signal is detected by a black and white CCD camera through a microscope objective so that a radiograph of the cell can be recorded. This imaging setup helps us to understand the sample location and to scan the sample position precisely (Figure

1). Diffraction and imaging modes can be interchanged by moving the entrance slits in or out of the X-ray path. A more detailed description of the T cup apparatus and imaging setup is described by *Wang et al.* [1998].

A schematic cell assembly used in this study is shown in Figure 2, together with a typical X-ray projection. Both polycrystalline Fe (maximum 800 μm in size and >99.99% purity; Goodfellow Co.) and pressure calibrant Au (1.5–3.0 μm and >99.96% purity; Alfa Aesar Co.) were mixed with MgO powder (ground from a single crystal, >99.9% purity; Goodfellow Co.) to inhibit grain growth. The sample and the pressure calibrant were packed in separate layers in the sample chamber, which was made of a mixture of amorphous boron and epoxy resin with the mixing ratio of 4:1 (by weight). The stacking direction was parallel to the diffraction vector so that the sample chamber can be scanned by X rays. A $W_{0.94}Re_{0.06}$-$W_{0.75}Re_{0.25}$ thermocouple was located at the sample and pressure calibrant interface, and diffraction data were collected from the sample and the pressure calibrant immediately adjacent the thermocouple. This minimizes the effect of any temperature and pressure gradients in the cell. Both sample and calibrant are simultaneously heated by an internal resistance heater made of a mixture of TiC and diamond powder (1:1 by weight). To avoid heat loss, LaCrO$_3$ semisintered plates were employed as a thermal insulator and placed between the heater
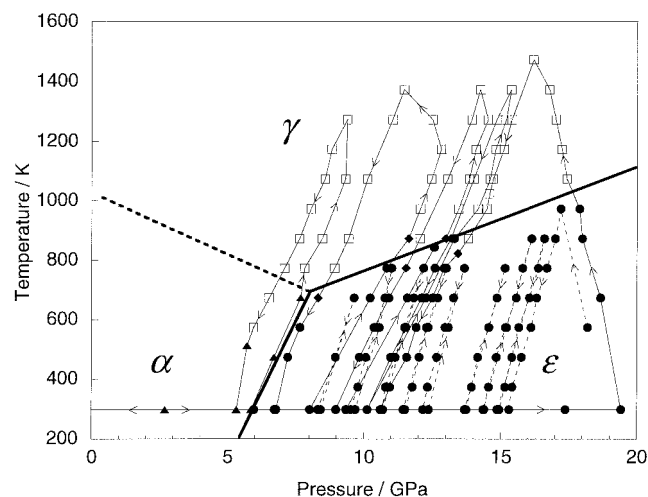
Figure 3. Phase diagram of Fe determined by in situ X-ray diffraction, together with experimental *P*-*T* paths. Triangles, circles, and squares show which phase (α, ε, or γ) is dominant under corresponding pressure and temperature condition. Diamonds represent the data points where the dominant phase is inconclusive. Thin solid and dashed lines indicate first run (T0105) to see the phase boundary and second run (T0134) for *P*-*V*-*T* measurement of ε-Fe, respectively. Arrows show directions of pressure and temperature traverses. Sample was first squeezed to 20 GPa and heated to desired temperature. The heating and cooling cycles are repeated several times. This minimizes the random error caused by run-to-run differences in cells. Temperature fluctuation was only ~5 K at 1500 K.

and the semisintered, Co-doped MgO pressure medium with 30% porosity. Under high pressures the gaps between the inner cubic anvils were reduced, limiting the access to the sample and pressure marker. Assembly errors and erroneous dimensions in cell parts will cause the sample to be shadowed by the anvils or lead to experimental failure such as a blow out. To avoid these, all of the cell parts were made carefully using a miniature computerized numerical control (CNC) machine (PNC-300: Roland Co.), with linear dimensions accurate to within 30 μm.

Two experiments (runs T0105 and T0134) were performed. In the first run (Figure 3) Fe was compressed to 20 GPa and then heated to 1500 K. To determine the stability field of the Fe phases, we monitored phase changes on heating and cooling cycles at a constant load. This technique works best for boundaries that are subparallel to the *P* axis, such is the case for the ε-γ transition. For boundaries that are subparallel to the *T* axis, such as in the case of the α-ε boundary, isothermal compression/decompression is a better technique. At each *P* and *T* condition the diffraction profile was taken from the sample first, and then the calibrant pattern was taken to determine the pressure. Then the sample X-ray pattern was collected again without changing *P* and *T*. The exposure time was typically 5 min for each pattern. We compared diffraction intensities of the phases before and after pressure determination with a typical time interval of 6 min. The growing phase (whose intensity increases) was taken as the stable phase at the given *P*-*T* condition.

During heating cycles we can completely convert the sample to γ-Fe (Figure 4c). The 200 diffraction line of γ-Fe is quite intense and is isolated from other peaks. The ε-γ phase boundary can be clearly recognized by the appearance of the 200

peaks of γ-Fe and the disappearance of ε-Fe peaks. During cooling cycles the appearance of ε-Fe peaks is used to identify the ε-γ phase boundary. As we completely convert the sample to γ-Fe during heating cycle, it is fairly straightforward to recognize newly growing ε-Fe peaks. In some cases near the boundary, it is difficult to identify the growing phase in the 6-min interval, and these points we identify with solid diamonds in Figure 3. Heating and cooling cycles were repeated several times to clarify the stability field of each phase.

In the second run, *P*-*V*-*T* data were collected only in the ε phase stability field determined in the first run (Figure 3). As described by *Wang et al.* [1996], volume data were taken only after heating to minimize nonhydrostatic stress. Ideally, the sample should be heated over 1000 K to release the nonhydrostatic stress [*Wang et al.*, 1996], but in the present study, ε-Fe is stable only to lower temperatures. In addition, contamination by the γ phase diffraction lines would reduce the num-
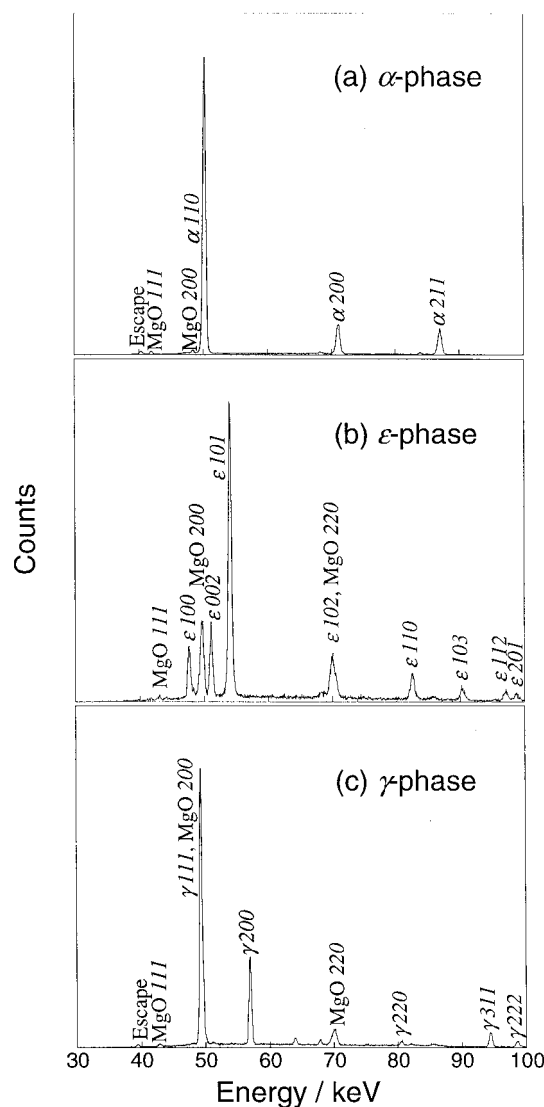

Figure 4. Representative X-ray diffraction patterns of Fe for (a) α (bcc) at ambient condition, (b) ε (hcp) at 18.0 GPa and 873 K, and (c) γ (fcc) at 15.1 GPa and 1173 K. Some Fe peaks overlap with MgO peaks, but only peaks from Fe and MgO are observed. Identification of each diffraction peak is shown. Exposure time was typically 300 s.

ber of diffraction peaks of the ε phase to be analyzed for volume calculation, and the coexistence of two or more phases associated with a phase transition can cause volume anomalies due to the difference in linear compressibility and the thermal expansivity [e.g., *Hamaya and Akimoto*, 1981]. Thus the maximum temperature was kept at 1000 K. Diffraction lines of the 111, 200, 220, 311, and 222 peaks from Au were used to determine pressure [*Anderson et al.*, 1989], whereas the 100, 002, 101, 110, and 103 lines of ε-Fe were used to obtain cell volumes throughout the experiment. Table 1 lists the cell parameters of ε-Fe under pressure and temperature conditions for the second run. The error range in the second run is quite similar to that of the first run, which can be estimated at several *P* and *T* conditions using the same peaks. This result indicates that the stress condition in both runs is not significantly different, although highest temperature was kept below 1000 K.

3. Results

3.1. Phase Relations

Representative X-ray diffraction profiles are shown in Figure 4 for the α, ε, and γ phases of Fe. Some MgO peaks overlap with Fe peaks, but no peaks other than Fe and MgO are present. After successive data collection during cooling, some peaks of the γ phase persisted even at room temperature in the first run (T0105). Overlap of the ε and γ phases sometimes causes anomalies in the lattice constants [e.g., *Hamaya and Akimoto*, 1981]. Thus no data point in the first run is used to construct the EOS of ε-Fe. After releasing pressure, Fe transformed back to the α phase without any trace of reaction in both runs.

Transformation boundaries between the ε and γ phases thus determined are drawn in Figure 3. Our data indicate that the triple point of the α, ε, and γ phases is located at 8.0(3) (value in parentheses indicates uncertainty, e.g., 8.0(3) means 8.0 ± 0.3) GPa and 680(50) K, which is close to that determined by a previous study using a cubic anvil high-pressure apparatus (8.3 GPa and 713 K) [*Akimoto et al.*, 1987] after carefully taking into account the effects of time dependence due to transition kinetics by repeating heating and cooling cycles. The slope of the phase boundary is 36(3) K GPa^{-1}, which is steeper than that reported by *Boehler et al.* [1987] in the DAC (24 K GPa^{-1}) but is in excellent agreement with the results obtained by cubic anvil press [*Akimoto et al.*, 1987] (34 K GPa^{-1}; as estimated from Akimoto et al.'s Figure 2) and the DAC results reported by *Mao et al.* [1987] (35 K GPa^{-1}). *Boehler et al.* [1987] adopted the α-ε-γ triple point at higher pressure and temperature (11.0 GPa and 773 K) and thus biased the slope. In the higher-pressure region (where their data were obtained) the data reported by *Boehler et al.* [1987] are also consistent with the extrapolation of our phase boundary.

At room temperature the α-ε phase boundary exhibits large hysteresis due to the slow kinetics by low temperature [e.g., *Von Bargen and Boehler*, 1990; *Taylor et al.*, 1991]. When the sample is compressed at room temperature, the α to ε transformation starts at above 11 GPa, while the back transformation starts at 11–8 GPa on pressure release [e.g., *Von Bargen and Boehler*, 1990; *Taylor et al.*, 1991]. Most of the previous work was carefully performed at room temperature. Differences in the transition pressure should be linked to nonhydrostaticity caused by differences in the solid pressure transmitting

medium used. In the present study, the α to ε transformation was found at ~11 GPa, while the ε to α transformation was detected at around 6 GPa. During compression at room temperature the sample should have experienced nonhydrostatic stress, and thus such data points were not used to constrain the phase boundary. In terms of the ε to α transformation the sample was cooling down from higher temperature right before the reversal transformation from ε to α at room temperature. The ε phase therefore should be regarded as the thermodynamically stable phase at 7.5 GPa and 580 K. No peaks from the α phase were detected during further cooling (Figure 3); however, these data points might be metastable due to the lack of transition energy. Thus the α-ε boundary is less well constrained and requires further isothermal compression/decompression experiments. On the basis of our preliminary data, however, the boundary appears to have a positive slope, consistent with results from *Akimoto et al.* [1987], whose measurements were made at elevated temperature.

3.2. Room Temperature Equation of State of ε-Fe

We fit our room temperature *P-V* data with the third-order Birch-Murnaghan EOS, which is represented by

$$P(V) = (3/2) K_{T,0} \left[\left(\frac{V_0}{V} \right)^{7/3} - \left(\frac{V_0}{V} \right)^{5/3} \right]$$

$$\cdot \left\{ 1 - (3/4)(4 - K'_{T,0}) \left[\left(\frac{V_0}{V} \right)^{2/3} - 1 \right] \right\}, \qquad (1)$$

where $K_{T,0}$, $K'_{T,0}$, and V_0 are isothermal bulk modulus, its pressure derivative, and unit cell volume, respectively, at the ambient condition. Room temperature data taken after the heating and cooling cycles are shown in Figure 5 (inset), and the fit is represented by the solid line. Because of the limited compression range (10%) and the unknown V_0, fitting results can vary because of the well-known trade-off among $K_{T,0}$, $K'_{T,0}$, and V_0, which is shown in Figure 6, together with previous room temperature data [*Jephcoat et al.*, 1986; *Mao et al.*, 1990; *Dubrovinsky et al.*, 1998a] in the DAC. Table 2 summarizes the EOS parameters. In Table 2 the EOS parameters of *Jephcoat et al.* [1986] are recalculated by excluding lower-pressure data (below 18 GPa) because the trend of these data does not follow that of ε-Fe but becomes closer to that of α-Fe as can be seen in Jephcoat et al.'s Figure 2. Compared to previous data, our data show that the resultant V_0 tends to be slightly higher and $K_{T,0}$ tends to be lower. Our data, obtained at lower pressures with higher precision, help to better define $K_{T,0}$. On the other hand, the limited pressure range does not provide robust constraints on $K'_{T,0}$. Therefore we combine our data with those obtained by *Jephcoat et al.* [1986] and *Mao et al.* [1990] and fit the whole data set to (1). This yields $K_{T,0} = 135(19)$ GPa, $K'_{T,0} = 6.0(4)$, and $V_0 = 22.7(3)$ Å^3. These parameters are consistent with our data series in Figure 6. On the other hand, data reported by *Dubrovinsky et al.* [1998a] give lower V_0 (22.2(1) Å^3) and $K'_{T,0}$ (4.9(4)) values as shown by the dotted line in Figure 5 (inset), although the room temperature parameters reported by *Mao et al.* [1990] were used for further fitting of the high-temperature data of *Dubrovinsky et al.* [1998a]. We note that *Dubrovinsky et al.* [1998a], did not determine pressure in situ at high temperatures, but rather determined pressure before and after heating. The unknown thermal pressure and relaxation in gaskets at higher tempera-

Table 1. Unit Cell Parameters of ε-Fe at Various Pressure and Temperature Conditions for Run T0134[a]

T,K	P,GPa	Au V/V_0	Fe a,Å	Fe c,Å	Fe V,Å³	Fe c/a
573.0	18.19 (27)	0.9238	2.4610	3.9557	20.75 (12)[b]	1.6074
973.0	17.20 (3)	0.9373	2.4727	4.0045	21.20 (11)	1.6195
873.0	16.99 (14)	0.9357	2.4719	3.9995	21.16 (11)	1.6180
773.0	16.69 (14)	0.9345	2.4696	3.9931	21.09 (11)	1.6169
673.0	16.31 (8)	0.9330	2.4679	3.9874	21.03 (11)	1.6157
573.0	16.10 (13)	0.9316	2.4664	3.9813	20.97 (11)	1.6142
473.0	15.75 (5)	0.9305	2.4650	3.9774	20.93 (11)	1.6136
373.0	15.41 (2)	0.9293	2.4632	3.9742	20.88 (11)	1.6134
298.0	15.31 (8)	0.9281	2.4626	3.9711	20.86 (11)	1.6126
298.0	14.90 (19)	0.9294	2.4627	3.9728	20.87 (11)[b]	1.6132
873.0	16.60 (17)	0.9371	2.4726	4.0007	21.18 (11)	1.6180
773.0	16.37 (13)	0.9354	2.4709	3.9933	21.11 (11)	1.6161
673.0	16.05 (17)	0.9343	2.4688	3.9892	21.06 (11)	1.6159
573.0	15.66 (13)	0.9332	2.4667	3.9837	20.99 (11)	1.6150
473.0	15.41 (14)	0.9317	2.4661	3.9796	20.96 (11)	1.6137
373.0	15.15 (24)	0.9299	2.4644	3.9755	20.91 (11)	1.6131
298.0	14.94 (21)	0.9291	2.4635	3.9740	20.89 (12)	1.6131
298.0	14.35 (32)	0.9313	2.4646	3.9753	20.91 (11)[b]	1.6129
573.0	15.21 (22)	0.9346	2.4697	3.9869	21.06 (12)[b]	1.6143
873.0	16.13 (17)	0.9387	2.4741	4.0049	21.23 (12)	1.6187
773.0	15.80 (19)	0.9377	2.4727	3.9966	21.16 (11)	1.6163
673.0	15.56 (24)	0.9361	2.4705	3.9932	21.11 (12)	1.6163
573.0	15.17 (21)	0.9348	2.4686	3.9876	21.04 (12)	1.6153
473.0	14.84 (25)	0.9338	2.4669	3.9841	21.00 (12)	1.6150
373.0	14.55 (28)	0.9325	2.4664	3.9770	20.95 (12)	1.6125
298.0	14.39 (24)	0.9314	2.4644	3.9756	20.91 (11)	1.6132
298.0	13.67 (29)	0.9339	2.4669	3.9782	20.97 (11)[b]	1.6126
573.0	14.55 (29)	0.9376	2.4709	3.9896	21.10 (11)[b]	1.6146
773.0	15.15 (21)	0.9405	2.4742	4.0015	21.21 (11)	1.6173
673.0	14.85 (18)	0.9393	2.4723	3.9956	21.15 (11)	1.6161
573.0	14.57 (23)	0.9374	2.4717	3.9898	21.11 (12)	1.6142
473.0	14.15 (27)	0.9365	2.4693	3.9875	21.06 (12)	1.6148
373.0	13.93 (25)	0.9348	2.4685	3.9823	21.02 (12)	1.6133
298.0	13.73 (31)	0.9338	2.4670	3.9789	20.97 (11)	1.6128
298.0	12.36 (27)	0.9392	2.4726	3.9870	21.11 (12)[b]	1.6124
573.0	13.08 (31)	0.9434	2.4766	3.9996	21.24 (12)[b]	1.6150
773.0	13.66 (35)	0.9470	2.4818	4.0106	21.39 (11)	1.6160
673.0	13.27 (28)	0.9459	2.4794	4.0060	21.33 (12)	1.6157
573.0	12.97 (40)	0.9440	2.4782	4.0001	21.28 (12)	1.6141
473.0	12.66 (39)	0.9428	2.4764	3.9971	21.23 (12)	1.6140
373.0	12.33 (41)	0.9414	2.4750	3.9927	21.18 (12)	1.6132
298.0	12.16 (45)	0.9402	2.4738	3.9896	21.14 (12)	1.6127
298.0	11.44 (26)	0.9429	2.4761	3.9939	21.21 (12)[b]	1.6130
573.0	12.29 (21)	0.9466	2.4800	4.0044	21.33 (11)[b]	1.6147
773.0	13.01 (18)	0.9495	2.4856	4.0186	21.50 (12)	1.6167
673.0	12.69 (20)	0.9482	2.4830	4.0134	21.43 (12)	1.6164
573.0	12.35 (19)	0.9468	2.4815	4.0073	21.37 (12)	1.6149
473.0	12.01 (19)	0.9452	2.4795	4.0026	21.31 (12)	1.6143
373.0	11.77 (15)	0.9438	2.4782	3.9985	21.27 (12)	1.6135
298.0	11.51 (22)	0.9428	2.4774	3.9947	21.23 (12)	1.6125
298.0	10.70 (16)	0.9462	2.4800	4.0002	21.31 (12)[b]	1.6130
573.0	11.53 (25)	0.9505	2.4833	4.0111	21.42 (11)[b]	1.6152
773.0	12.18 (14)	0.9530	2.4887	4.0258	21.59 (12)	1.6176
673.0	11.82 (14)	0.9520	2.4868	4.0197	21.53 (12)	1.6164
573.0	11.49 (13)	0.9507	2.4857	4.0132	21.47 (12)	1.6145
473.0	11.14 (17)	0.9491	2.4829	4.0087	21.40 (11)	1.6145
373.0	10.79 (20)	0.9477	2.4814	4.0057	21.36 (12)	1.6143
298.0	10.66 (18)	0.9463	2.4825	4.0022	21.36 (13)	1.6122
298.0	9.69 (16)	0.9506	2.4843	4.0072	21.42 (12)[b]	1.6130
573.0	10.56 (14)	0.9549	2.4886	4.0205	21.56 (12)[b]	1.6156
773.0	11.02 (11)	0.9588	2.4937	4.0327	21.72 (12)	1.6171
673.0	10.76 (10)	0.9571	2.4917	4.0280	21.66 (12)	1.6166
573.0	10.46 (14)	0.9554	2.4891	4.0231	21.59 (12)	1.6163
473.0	10.08 (13)	0.9541	2.4878	4.0135	21.51 (11)	1.6132
373.0	9.78 (11)	0.9527	2.4859	4.0128	21.47 (12)	1.6142
298.0	9.52 (15)	0.9513	2.4848	4.0098	21.44 (12)	1.6137
298.0	8.43 (13)	0.9561	2.4881	4.0170	21.54 (12)[b]	1.6144
673.0	9.64 (10)	0.9624	2.4957	4.0366	21.77 (12)	1.6174
473.0	8.96 (11)	0.9591	2.4930	4.0252	21.66 (12)	1.6146
298.0	8.32 (14)	0.9567	2.4893	4.0178	21.56 (12)	1.6140
298.0	6.72 (5)	0.9643	2.4946	4.0237	21.68 (15)[b]	1.6130
298.0	5.98 (8)	0.9680	2.4959	4.0233	21.71 (15)[b]	1.6120

[a]Values in parentheses are uncertainties, e.g., 18.19 (27) means 18.19 ± 0.27.
[b]Data are collected during heating cycles. These data points are not used for any room temperature and high-temperature curve fitting.

ture may have contributed to pressure uncertainty. Thus *Dubrovinsky et al.*'s [1998a] data are not included in the Birch-Murnaghan EOS fit. The preferred EOS is shown as the solid line in Figure 5. Subsequent high-temperature EOS fitting is therefore carried out using this preferred EOS as the reference base line.

3.3. High Pressure and High Temperature EOS of ε-Fe

Three different high-temperature EOSs are employed to extract thermoelastic properties of ε-Fe: (1) the high-temperature Birch-Murnaghan EOS, (2) the thermal pressure EOS [*Anderson*, 1980, 1984; *Anderson et al.*, 1989], and (3) the Mie-Grüneisen-Debye EOS.

The high-temperature Birch-Murnaghan EOS is an extension of the room temperature EOS and is represented by

$$P(V, T) = (3/2) K_{T,0} \left[\left(\frac{V_{T,0}}{V} \right)^{7/3} - \left(\frac{V_{T,0}}{V} \right)^{5/3} \right]$$
$$\cdot \left\{ 1 - (3/4)(4 - K'_{T,0}) \left[\left(\frac{V_{T,0}}{V} \right)^{2/3} - 1 \right] \right\}, \quad (2)$$

where $K_{T,0}$, $K'_{T,0}$, and $V_{T,0}$ denote zero-pressure isothermal bulk modulus, its pressure derivative, and unit cell volume, respectively, at a temperature T. Assuming that the second- and higher-order pressure derivatives of the bulk modulus are negligible, then $K_{T,0}$ and $K'_{T,0}$ are given by

$$K_{T,0} = K_0 + (\partial K_{T,0}/\partial T)_P (T - 300) \quad (3)$$

$$K'_{T,0} = K'_0, \quad (4)$$

where K_0 and K'_0 are taken at zero pressure. The temperature derivative of the bulk modulus $(\partial K_{T,0}/\partial T)_P$ is assumed constant and represents an average property throughout the P and T range of this study. From the definition of thermal expansivity $\alpha_{T,0}$, zero-pressure volume $V_{T,0}$ is expressed as

Figure 6. Trade-off diagram of (a) K_0 versus K'_0 and (b) V_0 versus K'_0. Also plotted are the results using individual data sets of *Mao et al.* [1990], *Jephcoat et al.* [1986], and *Dubrovinsky et al.* [1998a], respectively.

$$V_{T,0} = V_0 \exp \int_{300}^{T} \alpha_{T,0} \, dT, \quad (5)$$

where $\alpha_{T,0}$ is empirically represented by

$$\alpha_{T,0} = a + bT - cT^{-2}, \quad (6)$$

where a, b, and c are positive constants. We use our room temperature Birch-Murnaghan EOS as the reference baseline in the high-temperature data fit. A total of 55 data points collected during cooling cycles are fit to the high-temperature Birch-Murnaghan EOS, yielding values for the three parameters, $(\partial K_{T,0}/\partial T)_P$, a, and b of $-4.48(56) \times 10^{-2}$ GPa K^{-1}, $3.98(24) \times 10^{-5}$ K^{-1}, and $5.07(88) \times 10^{-8}$ K^{-2}, respectively. Including parameter c results in an ill-conditioned array in the least squares fit; thus c is fixed at zero. The fitting results are illustrated as the solid (298, 473, 673, and 873 K) and the dashed (373, 573, 773, 973 K) curves together with the estimated maximum error in Figure 7. On the whole, the fitting reproduces the cell volume data quite well.

In a recent high-temperature DAC study, *Dubrovinsky et al.* [1998a] obtained *P-V-T* data for ε-Fe up to 68 GPa and 1700 K. They adopted $K_0 = 164(3)$ GPa, $K'_0 = 5.36(16)$, $V_0 = 6.76(2)$ cm^3 mol^{-1} ($=22.45(7)$ Å^3) to calculate the other four parameters in the high-temperature Birch-Murnaghan EOS fit and reported $(\partial K_{T,0}/\partial T)_P = -4.3(3) \times 10^{-2}$ GPa K^{-1}, $a = 5.7(4) \times 10^{-5}$ K^{-1},
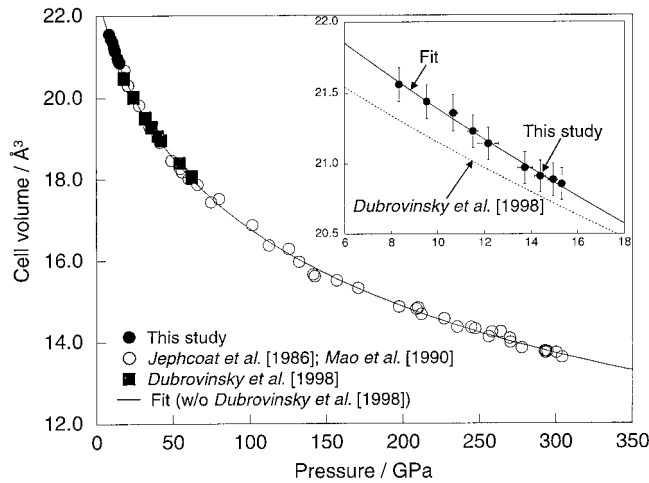

Figure 5. Cell volume of ε-Fe as a function of pressure at room temperature. Solid line represents a result from least squares fitting to third-order Birch-Murnaghan EOS. Data from *Dubrovinsky et al.* [1998a] show a slightly different trend (inset). Fitted solid line excludes the data from *Dubrovinsky et al.* [1998a].
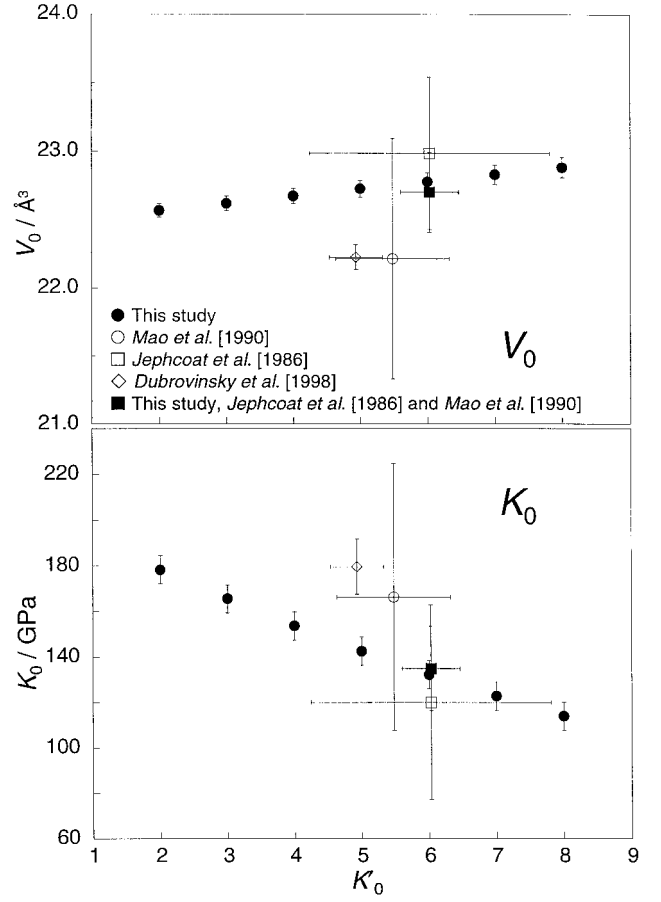
Table 2. Comparison of Room Temperature EOS Parameters[a]

	Mao et al. [1990]	*Jephcoat et al.* [1986][b]	*Dubrovinsky et al.* [1998]	This Study (Without Any Constraint)	Combined Values[c]
$K_{T,0}$	166 (58)	120 (43)	180 (12)	164 (93)	135 (19)
$K'_{T,0}$	5.5 (8)	6.0 (18)	4.9 (4)	3.1 (76)	6.0 (4)
V_0	22.2 (9)	23.0 (6)	22.2 (1)	22.6 (4)	22.7 (3)
R	0.9977	0.9988	0.9998	0.9966	0.9991

[a]Values in parentheses are uncertainties, e.g., 166 (58) means 166 ± 58.
[b]The data collected bellow 18 GPa are excluded. Calculation was done based on room temperature Birch-Murnaghan EOS.
[c]EOS parameters were derived by combining our data with that of *Jephcoat et al.* [1986] and *Mao et al.* [1990].

$b = 4.2(4) \times 10^{-9}$ K^{-2}, and $c = 0.17(7)$ K. Their $(\partial K_{T,0}/\partial T)_P$ value is consistent with our data, but their thermal expansivity value is not. Their thermal expansivity is higher than our data by 9% at room temperature. On the other hand, at 800 K our thermal expansion is much higher by 25% due to the very large b.

The thermal pressure EOS [*Anderson*, 1980, 1984; *Anderson et al.*, 1989] is based on Mie-Grüneisen theory and is represented by [*Jackson and Rigden*, 1996]

$$P(V, T) = P(V, T_0) + \Delta P_{th} = \sum b_i X_i(\eta, T), \quad (7)$$

where

$\eta = V_0/V$,

$X_1 = \eta^{7/3} - \eta^{5/3} \qquad b_1 = 3K_T(V_0, T_0)/2$,

$X_2 = X_1(\eta^{2/3} - 1) \qquad b_2 = \frac{9}{8} K_T(V_0, T_0)[K'_{T0}(V_0, T_0) - 4]$,

$$P(V, T_0) = b_1 X_1 + b_2 X_2, \quad (8)$$

$X_3 = (T - T_0) \qquad b_3 = \alpha K_T$,

$X_4 = -(T - T_0) \ln \eta \quad b_4 = (\partial K_T/\partial T)_V$,

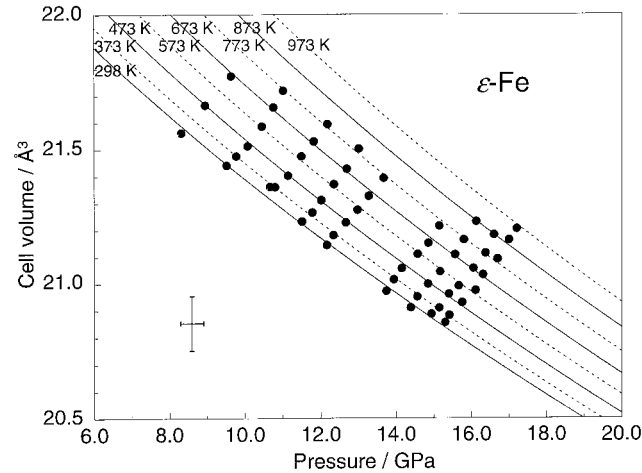$X_5 = (T - T_0)^2 \qquad b_5 = [(\partial^2 P/\partial T^2)_V]/2$,

Figure 7. High-temperature Birch-Murnaghan equation of state fit for ε-Fe. Solid lines and dashed lines are drawn every other 100 K, except for the 298 K line. Estimated error bars (maximum) on the P-V-T measurements are shown in lower left-hand corner and denote typical standard deviation of each data point. However, the close agreement between the data and the fits suggests much smaller uncertainties (comparable to symbol size). High-temperature data collected during cooling cycle is used for the fit, and any data points collected during heating cycle are not included.
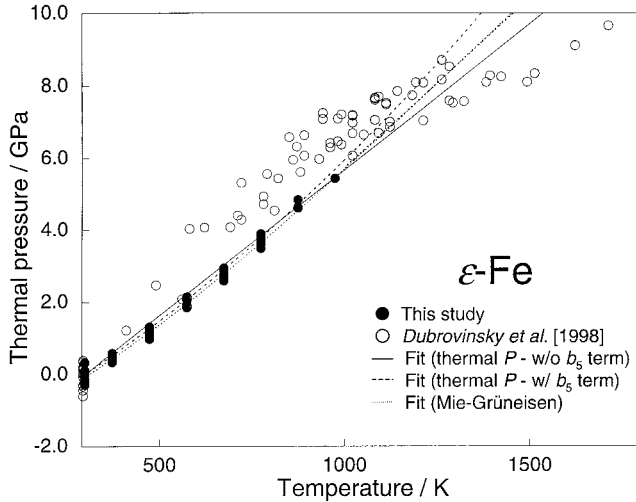
where the sum of the first and second terms in (7) represents the room temperature third-order Birch-Murnaghan EOS and the sum of the rest represents the thermal pressure P_{th}. The volume dependence of P_{th} is given by the term $b_4 X_4$. However, P_{th} is virtually volume-independent at constant T. Indeed, $(\partial K_T/\partial T)_V$ is not resolvable from zero in our least squares fit, and therefore b_4 is fixed at zero. Thus only the parameters in the third and fifth terms are determined by the fitting. Least squares fit to (7) gives $\alpha K_{T,0} = 6.88(30) \times 10^{-3}$ GPa K^{-1} and $(\partial^2 P/\partial T^2)_V = 4.63(53) \times 10^{-6}$ GPa K^{-1}. The $\alpha K_{T,0}$ value thus obtained is consistent with that from the high-temperature Birch-Murnaghan fit (7.15×10^{-3} GPa K^{-1}). Note that if $b_4 = (\partial K_T/\partial T)_V = 0$, then

$$(\partial K_T/\partial T)_P = -\alpha K_T K'_T \quad (9)$$

according to the thermodynamic relation

$$(\partial K_T/\partial T)_V = (\partial K_T/\partial T)_P + \alpha K_T(\partial K_T/\partial P)_T. \quad (10)$$

Thus the Anderson-Grüneisen parameter $\delta_T = -(\partial K_T/\partial T)_P/\alpha K_T = K'_T = 6.1$. Assuming that δ_T remains constant, from the relation

$$(\alpha/\alpha_0) = (V/V_0)^{\delta_T}, \quad (11)$$

thermal expansivity α is calculated as a function of V. The volume dependence of thermal expansivity can be compared to the data reported by *Funamori et al.* [1996] and *Dubrovinsky et al.* [2000]. *Funamori et al.* [1996] reported the thermal expansivities to be 3.88×10^{-5} K^{-1} and 3.16×10^{-5} K^{-1} as an average between 300 and 1000 K at the volume ratio V/V_0 of 0.905 and 0.890, while *Dubrovinsky et al.* [2000] reported them to be 4.31×10^{-5} K^{-1} and 3.65×10^{-5} K^{-1} at the same pressures, respectively. Our data are in general agreement with these data within the experimental uncertainty.

For the parameters obtained from the high-temperature Birch-Murnaghan EOS we may cross-check their validity using (9). Indeed, $(\partial K_T/\partial T)_P$ ($= -0.043$ GPa K^{-1}) obtained in the high-temperature Birch-Murnaghan fit agrees with $-\alpha K_T K'_T$ ($= -0.044$ GPa K^{-1}).

The Mie-Grüneisen-Debye EOS is in the following forms [*Jackson and Rigden*, 1996]:

$$P(V, T) = P(V, T_0) + \Delta P_{th}, \quad (12)$$

$$\Delta P_{th} = \left(\frac{\gamma}{V}\right)[E(T, \theta_D) - E(T_0, \theta_D)], \quad (13)$$

$$E = 9nRT\left(\frac{T}{\theta_D}\right)^3 \int_0^{\theta_D} t^3 \, dt/(e^t - 1), \quad (14)$$

Figure 8. Thermal pressure of ε-Fe up to 20 GPa and 1000 K, together with *Dubrovinsky et al.*'s [1998a] data. The 55 cooling cycle data points in Table 1 are fitted to *Anderson*'s [1980, 1984] thermal pressure approach with (dashed line) and without $(\partial^2 P/\partial T^2)_V$ term (solid line) and Mie-Grüneisen-Debye approach (dotted line). The best fit to our data is obtained with the Mie-Grüneisen-Debye equations within this temperature range. Above the Debye temperature of 998 K, dotted line shows the extrapolation based on a linear function.

where E is internal thermal energy, θ_D is Debye temperature, γ is Grüneisen parameter, n is the number of atoms per chemical formula, and R is the gas constant. The volume dependence of θ_D and γ is given by

$$\theta_D = (\theta_D)_0 \left(\frac{V}{V_0}\right)^{-\gamma} \qquad (15)$$

$$\gamma = \gamma_0 \left(\frac{V}{V_0}\right)^q, \qquad (16)$$

where q is a fitting parameter. Thus, in the Mie-Grüneisen-Debye EOS the number of parameters is 5 (K_0, K_0', $(\theta_D)_0$, γ_0, and q). In the present study, room temperature pressure $P(V, T_0)$ is again taken from the third-order Birch-Murnaghan EOS. Our 55 data points are fit to the Mie-Grüneisen-Debye EOS to yield $(\theta_D)_0 = 998(85)$ K, $\gamma_0 = 1.36(8)$, and $q = 0.91(7)$, respectively.

Figure 8 shows the fitting results for the thermal pressure EOS with and without b_5 term and the Mie-Grüneisen-Debye EOS as a function of temperature (solid line) together with our data and the data reported by *Dubrovinsky et al.* [1998a]. The thermal pressure EOS with the b_5 term has a slight curvature due to the positive $(\partial^2 P/\partial T^2)_V$ value. The *Dubrovinsky et al.* [1998a] data, on the other hand, show a large scatter with an opposite curvature and a weakly defined kink at ~800 K. One reason for this discrepancy may be the difference of volume ratio of *Dubrovinsky et al.* [1998a]. In their data, thermal pressure was measured mainly in the two different ranges in volume ratio. Volume ratios of 0.90–0.92 shifted toward the left-hand side of the thermal pressure plot, and its slope is slightly steeper than that of our data. On the other hand, volume ratios of 0.80–0.83 show shallower slope. As discussed before, the curvature observed by *Dubrovinsky et al.* [1998a] is unlikely to be an intrinsic feature of the thermal pressure of ε-Fe, since

their pressures were not obtained at high-temperature conditions.

The thermal pressure EOS without the b_5 term overestimates the thermal pressure below the Debye temperature and underestimates it above the Debye temperature. Of the three different approaches, Mie-Grüneisen-Debye EOS is perhaps most suitable in examining the thermal pressure variation with increasing temperature, as it adequately describes the nonlinear behavior observed in our data across the Debye temperature. Between the Debye temperature and 2000 K, the Mie-Grüneisen-Debye EOS predicts a linear temperature dependence of the thermal pressure, which is used to extrapolate the thermal pressure to higher temperatures. In Figure 8 the Mie-Grüneisen-Debye EOS is shown as the dotted line below Debye temperature of 998 K, and extrapolation of the thermal pressure is shown as the same dotted line above the Debye temperature as a linear function.

3.4. The c/a Ratio

The c/a ratio increases with temperature and decreases slightly with pressure. In order to model the pressure and temperature dependence on the a and c axes individually, each cell parameter is fit to the Mie-Grüneisen-Debye EOS based on a fictitious volume (a^3 or c^3) in the same way as in Figure 8. Linear incompressibility and thermal expansivity are then obtained by dividing the fictitious properties by 3. The linear thermal expansivity for the c axis is slightly larger than that of the a axis, while incompressibilities are quite similar. Thus the pressure dependence of c/a at each temperature is almost the same, although absolute values of c/a become higher with increase temperature. Figure 9 shows the c/a ratio change as a function of pressure and temperature, together with pseudo c/a ratios in the orthorhombic "β"-Fe reported by *Andrault et al.* [2000] and in the double-hcp (dhcp) "β"-Fe reported by *Saxena et al.* [1995] and the room temperature c/a ratios on the ε phase reported by *Jephcoat et al.* [1986] and *Mao et al.* [1990].
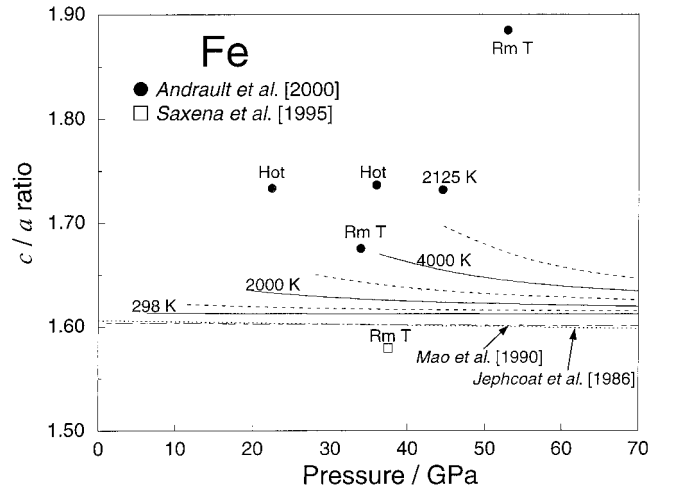

Figure 9. Comparison of c/a ratio as a function of pressure and temperature. Solid circles and open square show the pseudo c/a of the orthorhombic phase reported by *Andrault et al.* [2000] and the c/a of the dhcp phase reported by *Saxena et al.* [1995], respectively. Solid lines (298, 2000, and 4000 K) and dashed lines (1000, 3000, and 5000 K) show extrapolations of data from the present study. Room temperature c/a variations as a function of pressure [*Jephcoat et al.*, 1986; *Mao et al.*, 1990] are also plotted.
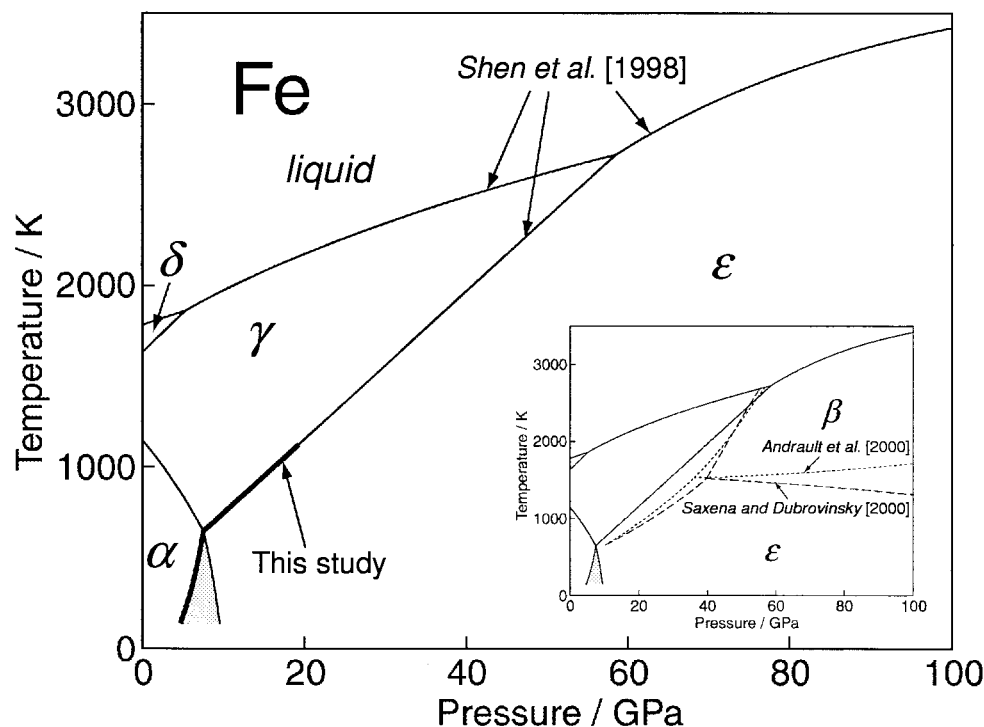
Figure 10. The phase diagram for Fe showing phase boundaries (heavy solid lines) obtained in this study. Shaded area indicates the possible *P* and *T* range where α-ε boundary exists. Our ε-γ phase boundary is identical with that reported by *Shen et al.* [1998] and shows no stability field of β phase. If the β phase exists, phase diagram need to be modified (inset). Dashed and dotted lines are the phase boundaries reported by *Saxena and Dubrovinsky* [2000] and *Andrault et al.* [2000], respectively.

The room temperature c/a ratio of ε-Fe is reported to decrease as a function of pressure ($c/a = 1.606(1) - 1.2(3) \times 10^{-4}P$ (GPa) [*Jephcoat et al.*, 1986]; and $c/a = 1.604(2) - 0.49(14) \times 10^{-4}P$ (GPa) [*Mao et al.*, 1990]). Our room temperature c/a is represented by $c/a = 1.613 - 1.6 \times 10^{-6}P$ (GPa) as linear function, which is 0.4–0.8% larger than that reported by *Jephcoat et al.* [1986] and *Mao et al.* [1990] at the pressure up to 200 GPa. However, from the scatter of the data in this study, *Jephcoat et al.* [1986], and *Mao et al.* [1990], the 0.4–0.8% difference in c/a should be regarded as within experimental error.

4. Discussion

4.1. Stability of ε-Fe at IOB Conditions

Numerous experimental and theoretical studies carried out on Fe in the past decade have suggested the existence of new phases of Fe. At pressures above 40 GPa, *Saxena and Dubrovinsky* [2000, and references therein] proposed a dhcp phase, whereas *Andrault et al.* [1997, 2000] reported an orthorhombic structure. Crystallographic assessments of this high-pressure phase, the so-called "β phase," not to be confused with the low-pressure β phase reported by *Mirwald and Kennedy* [1979] and *Besson and Nicol* [1990], are currently under intense debate [*Dubrovinsky et al.*, 1998b]. *Ross et al.* [1990] indicated that the high melting curve reported by *Williams et al.* [1987] can be accounted for by a bcc structure of Fe (different from the α phase) based on their theoretically calculated EOS. On the basis of molecular dynamics calculations, *Matsui and Anderson* [1997] pointed out a possibility of yet another new bcc phase that may be able to account for the

phase transition reported by *Brown and McQueen* [1986] in their shock experiments as the transformation from hcp to the bcc at 200 GPa and from the bcc to liquid at 243 GPa.

Figure 10 shows a phase diagram of Fe that summarizes the relevant experimental data. Our ε-γ boundary (heavy solid line with the slope of 36 K GPa^{-1}) is consistent with that reported by *Shen et al.* [1998], whose raw data, for clarity, are not shown in Figure 10. Our data and *Shen et al.*'s [1998] data show no stability field of β phase. If the β phase exists, the phase diagram needs to be modified (Figure 10 (inset)). *Andrault et al.* [2000] and *Saxena and Dubrovinsky* [2000] report shallower slopes of the ε-γ boundary.

The location of the proposed "β phase" stability field varies significantly. *Saxena and Dubrovinsky* [2000] report a negative β-ε slope, while *Andrault et al.* [2000] report a positive one (Figure 10 (inset)). The stability field reported by *Yoo et al.* [1996] obtained between 15 and 40 GPa (not shown in Figure 10) is in general agreement with that of *Saxena and Dubrovinsky* [2000]. *Andrault et al.* [2000] discussed the difference in the stability field studies and concluded that the new phase may be attributed to its metastability, probably due to temperature or pressure inhomogenity in the DAC. A metastable new phase could be a reasonable explanation for the fact that the "β" phases appear in the pressure range of 15–40 GPa in some experiments [*Yoo et al.*, 1996] but do not appear in other experiments [*Shen et al.*, 1998]. *Andrault et al.* [2000] also hypothesized the existence of a stability field for the new phase at pressures over 35 GPa, although this conclusion is inconsistent with the data obtained by *Shen et al.* [1998]. If the new β phase exists, the position and slope of the β-ε phase boundary are important in order to establish the state of Fe in the Earth's
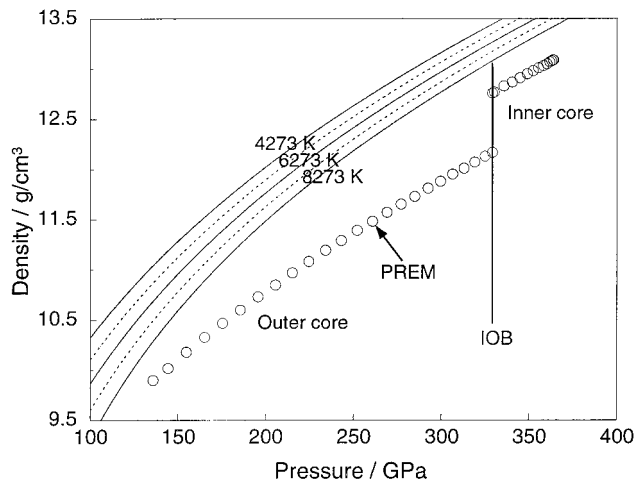
Figure 11. Density of ε-Fe at the Earth's core condition. Solid and dashed lines are obtained by extrapolation of the Mie-Grüneisen-Debye EOS. Open circles are PREM densities. The ε-Fe densities are significantly higher than those for PREM, supporting the existence of light element(s) in both the inner core and outer core.

core. However, the well-constrained ε-γ boundary from our data shows no indication of an ε-γ-β triple point and therefore argues against the existence of a stable β phase.

Another way to examine the existence of other phases of Fe is from the pressure and temperature dependence of the c/a ratio. As can be seen in Figure 9, the c/a ratio data for the three studies shown are inconsistent. The pseudo c/a of orthorhombic phase [*Andrault et al.*, 2000] is >5% larger than that of the ε phase, while the c/a (in terms of hcp) of the dhcp phase [*Saxena et al.*, 1995] is 5% smaller. *Andrault et al.* [1997, 2000] pointed out that the difference between the dhcp and orthorhombic phases is largely attributed to the interpretation of the diffraction patterns. However, the difference in c/a shown in Figure 9 is inconsistent with these phases being identical.

4.2. Density Under Inner Core Conditions

To discuss the density profile in the Earth's core, information about the thermal expansion of the corresponding Fe phase is indispensable as well as bulk modulus and its pressure derivative. Uncertainty in previous density discussions mainly comes from the lack of knowledge of the thermal expansivity [*Poirier*, 1994]. On the assumption that the inner core is composed of pure ε-Fe, extrapolation of our resultant Mie-Grüneisen-Debye EOS, which includes the information about both bulk modulus up to 300 GPa and thermal expansivity over 1000 K, allows us to estimate the density under the Earth's core condition. Figure 11 shows density of ε-Fe as a function of pressure along several isotherms, together with the density of PREM [*Dziewonski and Anderson*, 1981]. The solid (4273, 6273, and 8273 K) and dashed (5273 and 7273 K) lines indicate our density calculations based on Mie-Grüneisen-Debye EOS. Our density profile is in excellent agreement with that reported by *Dubrovinsky et al.* [2000]. In order for the density of pure ε-Fe to match that of PREM, core temperatures must be exceedingly high. Even when the highest available estimate of inner core and outer core boundary (IOB) temperature of 7600 K [*Williams et al.*, 1987] is employed, ε-Fe still has about 4% excess density compared to PREM. This result supports

the notion that light elements must be present not only in the outer core but also in the inner core [*Jephcoat and Olsen*, 1987].

5. Conclusions

In situ X-ray diffraction for Fe has been carried out up to 20 GPa and 1500 K in a multianvil apparatus. The α-ε-γ triple point is located at 8.0(3) GPa and 680(50) K, and the slope of the ε-γ phase boundary is 36(3) K GPa^{-1}. These data are consistent with previous results obtained in a cubic anvil apparatus [*Akimoto et al.*, 1987]. Combined with data from diamond anvil cell experiments, room temperature volume data yield a third-order Birch-Murnaghan EOS with $K_0 = 135(19)$ GPa, $K'_0 = 6.0(4)$, and $V_0 = 22.7(3)$ Å^3. Equations of state based on high-temperature Birch-Murnaghan, Mie-Grüneisen-Debye, and thermal pressure approach based on Mie-Grüneisen theory, are all consistent in the investigated pressure and temperature range. The temperature and pressure dependences of the c/a ratio support the notion of ε-Fe being the stable phase under the conditions of the Earth's core. Calculated densities from the Mie-Grüneisen-Debye EOS are significantly higher than those of PREM, assuming core temperatures proposed to date. The density data can be most readily made consistent with PREM by the presence of light elements in both the outer and inner core.

References

Akimoto, S., T. Suzuki, T. Yagi, and O. Shimomura, Phase diagram of iron determined by high-pressure/temperature X-ray diffraction using synchrotron radiation, in *High-Pressure Research in Mineral Physics*, *Geophys. Monogr. Ser.*, vol. 39, edited by M. H. Manghnani and Y. Syono, pp. 149–154, AGU, Washington, D. C., 1987.

Anderson, O. L., An experimental high-temperature thermal equation of state by passing the Gruneisen parameter, *Phys. Earth Planet. Inter.*, 22, 173–183, 1980.

Anderson, O. L., A universal equation of state, *J. Geodyn.*, 1, 185–214, 1984.

Anderson, O. L., *Equations of State for Solids in Geophysics and Ceramic Science*, pp. 258–259, Oxford Univ. Press, New York, 1995.

Anderson, O. L., and D. G. Isaak, Calculated melting curves for phase of iron, *Am. Mineral.*, 85, 376–385, 2000.

Anderson, O. L., D. G. Isaak, and S. Yamamoto, Anharmonicity and the equation of state for gold, *J. Appl. Phys.*, 65, 1534–1543, 1989.

Andrault, D., G. Fiquet, M. Kunz, F. Visocekas, and D. Häusermann, The orthorhombic structure of iron: An in situ study at high-temperature and high-pressure, *Science*, 278, 831–834, 1997.

Andrault, D., G. Fiquet, T. Charpin, and T. le Bihan, Structure analysis and stability field of β-iron at high *P* and *T*, *Am. Mineral.*, 85, 364–371, 2000.

Basinski, Z. S., W. Hume-Rothery, and A. L. Sutton, The lattice expansion of iron, *Proc. R. Soc. London, Ser. A*, 229, 459–467, 1955.

Besson, J. M., and M. Nicol, An equation of state of γ-Fe and some insights about magnetoelastic effects on measurements of the α-γ-ε triple point and other transitions, *J. Geophys. Res.*, 95, 21,717–21,720, 1990.

Birch, F., Elasticity and constitution of the Earth's interior, *J. Geophys. Res*., *57*, 227–286, 1952.

Birch, F., Density and composition of mantle and core, *J. Geophys. Res*., *69*, 4377–4388, 1964.

Boehler, R., Temperatures in the Earth's core from melting-point measurements of iron at high static pressures, *Nature*, *262*, 534–536, 1993.

Boehler, R., M. Nicol, and M. L. Johnson, Internally-heated diamond-anvil cell: Phase diagram and *P-V-T* of iron, in *High-Pressure Research in Mineral Physics*, *Geophys. Monogr. Ser.*, vol. 39, edited by M. H. Manghnani and Y. Syono, pp. 173–176, AGU, Washington, D. C., 1987.

Brown, J. M., and R. G. McQueen, Phase transitions, Grüneisen parameter, and elasticity for shocked iron between 77 GPa and 400 GPa, *J. Geophys. Res*., *91*, 7485–7494, 1986.

Dubrovinsky, L. S., S. K. Saxena, and P. Lazor, High-pressure and high-temperature in situ X-ray diffraction study of iron and corundum to 58 GPa using an internally heated diamond anvil cell, *Phys. Chem. Miner.*, *25*, 434–441, 1998a.

Dubrovinsky, L. S., S. K. Saxena, P. Lazor, H.-P. Weber, D. Andrault, G. Fiquet, M. Kunz, F. Visocekas, and D. Haüsermann, Structure of β-iron at high temperature and pressure, *Science*, *281*, 11, 1998b.

Dubrovinsky, L. S., S. K. Saxena, F. Tutti, S. Rekhi, and T. LeBehan, In situ X-ray study of thermal expansion and phase transition of iron at multimegabar pressure, *Phys. Rev. Lett.*, *84*, 1720–1723, 2000.

Dziewonski, A. M., and D. L. Anderson, Preliminary reference Earth model, *Phys. Earth Planet. Inter.*, *25*, 297–356, 1981.

Funamori, N., T. Yagi, and T. Uchida, High-pressure and high-temperature in situ X-ray diffraction study of iron above 30 GPa using MA8-type apparatus, *Geophys. Res. Lett.*, *23*, 953–956, 1996.

Hamaya, N., and S. Akimoto, Kinetics of pressure-induced phase transformation in KCl at room temperature, *High Temp. High Pressures*, *13*, 347–358, 1981.

Huang, E., W. A. Basset, and P. Tao, Study of bcc-hcp iron phase transition by synchrotron radiation, in *High-Pressure Research in Mineral Physics*, *Geophys. Monogr. Ser.*, vol. 39, edited by M. H. Manghnani and Y. Syono, pp. 165–172, AGU, Washington, D. C., 1987.

Jackson, I., and S. M. Rigden, Analysis of *P-V-T* data: Constraints on the thermoelastic properties of high-pressure minerals, *Phys. Earth Planet. Inter.*, *96*, 85–112, 1996.

Jephcoat, A., and P. Olsen, Is the inner core of the Earth pure iron?, *Nature*, *325*, 332–335, 1987.

Jephcoat, A. P., H. K. Mao, and P. M. Bell, Static compression of iron to 78 GPa with rare gas solids as pressure-transmitting media, *J. Geophys. Res.*, *91*, 4677–4684, 1986.

Laio, A., S. Bernard, G. L. Chiarotti, S. Scandolo, and E. Tosatti, Physics of iron at Earth's core conditions, *Science*, *287*, 1027–1030, 2000.

Manghnani, M. H., L. C. Ming, and N. Nakagiri, Investigation of the α-Fe ⇌ ε-Fe phase transition by synchrotron radiation, in *High-Pressure Research in Mineral Physics*, *Geophys. Monogr. Ser.*, vol. 39, edited by M. H. Manghnani and Y. Syono, pp. 155–163, AGU, Washington, D. C., 1987.

Mao, H. K., and P. M. Bell, Equations of state of MgO and ε Fe under static pressure conditions, *J. Geophys. Res.*, *84*, 4533–4536, 1979.

Mao, H. K., P. M. Bell, and C. Hadidiacos, Experimental phase relations of iron to 360 kbar, 1400°C, determined in an internally heated diamond-anvil apparatus, in *High-Pressure Research in Mineral Physics*, *Geophys. Monogr. Ser.*, vol. 39, edited by M. H. Manghnani and Y. Syono, pp. 135–138, AGU, Washington, D. C., 1987.

Mao, H. K., Y. Wu, L. C. Chen, J. F. Shu, and A. P. Jephcoat, Static compression of iron to 300 GPa and $Fe_{0.8}Ni_{0.2}$ alloy to 260 GPa: Implications for composition of the core, *J. Geophys. Res.*, *95*, 21,737–21,742, 1990.

Matsui, M., and O. L. Anderson, The case for a body-centered cubic phase (α′) for iron at inner core condition, *Phys. Earth Planet. Inter.*, *103*, 55–62, 1997.

Mirwald, P. W., and G. C. Kennedy, The Curie point and the α-γ transition of iron to 53 kbar: A reexamination, *J. Geophys. Res.*, *84*, 656–658, 1979.

Poirier, J.-P., Light elements in the Earth's outer core: A critical review, *Phys. Earth Planet. Inter.*, *85*, 319–337, 1994.

Rivers, M. L., T. S. Duffy, Y. Wang, P. J. Eng, S. R. Sutton, and G. Shen, A new facility for high-pressure research at the Advanced Photon Source, in *Properties of Earth and Planetary Materials at High Pressure and Temperature*, *Geophys. Monogr. Ser.*, vol. 101, edited by M. H. Manghnani and T. Yagi, pp. 79–86, AGU, Washington, D. C., 1998.

Ross, M., D. A. Young, and R. Grover, Theory of the iron phase diagram at Earth core conditions, *J. Geophys. Res.*, *95*, 21,713–21,716, 1990.

Saxena, S. K., and L. S. Dubrovinsky, Iron phases at high pressures and temperatures: Phase transition and melting, *Am. Mineral.*, *85*, 372–375, 2000.

Saxena, S. K., L. S. Dubrovinsky, P. Häggkvist, Y. Cerenius, G. Shen, and H. K. Mao, Synchrotron X-ray study of iron at high pressure and temperature, *Science*, *269*, 1703–1704, 1995.

Saxena, S. K., L. S. Dubrovinsky, and P. Häggkvist, X-ray evidence for the new phase β-iron at high temperature and high pressure, *Geophys. Res. Lett.*, *23*, 2441–2444, 1996.

Shen, G., H.-K. Mao, R. J. Hemley, T. S. Duffy, and M. L. Rivers, Melting and crystal structure of iron at high pressures and temperatures, *Geophys. Res. Lett.*, *25*, 373–376, 1998.

Stevenson, D. J., Models of the Earth's core, *Science*, *214*, 611–619, 1981.

Taylor, R. D., M. P. Pasternak, and R. Jeanloz, Hysteresis in the high pressure transformation of bcc-to-hcp-iron, *J. Appl. Phys.*, *69*, 6126–6128, 1991.

Vaughan, M. T., D. J. Weidner, Y. Wang, J. Chen, C. Koleda, and I. Getting, T-Cup: A new high-pressure apparatus for X-ray studies, *Rev. High Pressure Sci. Technol.*, *7*, 1520–1522, 1998.

Von Bargen, N., and R. Boehler, Effect of non-hydrostaticity on the α-ε transition of iron, *High Pressure Res.*, *6*, 133–140, 1990.

Wang, Y., D. J. Weidner, and F. Guyot, Thermal equation of state of $CaSiO_3$ perovskite, *J. Geophys. Res.*, *101*, 661–672, 1996.

Wang, Y., M. Rivers, S. Sutton, P. Eng, G. Shen, and I. Getting, A multi-anvil, high-pressure facility for synchrotron radiation research at GeoSoilEnviroCARS at the Advanced Photon Source, *Rev. High Pressure Sci. Technol.*, *7*, 1490–1495, 1998.

Williams, Q., R. Jeanloz, J. Bass, B. Svendsen, and T. J. Ahrens, The melting curve of iron to 250 gigapascals: A constraint on the temperature at Earth's center, *Science*, *236*, 181–182, 1987.

Yagi, T., and N. Funamori, Chemical composition of the lower mantle inferred from the equation of state of $MgSiO_3$ perovskite, *Philos. Trans. R. Soc. London, Ser. A*, *354*, 1371–1384, 1996.

Yoo, C. S., N. C. Holmes, M. Ross, D. J. Webb, and C. Pike, Shock temperatures and melting of iron at Earth core conditions, *Phys. Rev. Lett.*, *70*, 3931–3934, 1993.

Yoo, C. S., P. Söderlind, J. A. Moriarty, and A. J. Cambell, Dhcp as a possible new ε′ phase of iron at high pressures and temperatures, *Phys. Lett. A*, *214*, 65–70, 1996.

———————
M. L. Rivers, S. R. Sutton, T. Uchida, and Y. Wang, Consortium for Advanced Radiation Sources, University of Chicago, 5640 S. Ellis Ave., Chicago, IL 60637, USA. (rivers@cars.uchicago.edu; sutton@cars.uchicago.edu; uchida@cars.uchicago.edu; wang@cars.uchicago.edu)